remote sensing

MDPI

Article

Day and Night Retrieval of Layered Cloud Cover from Geostationary Satellite Observations

Junbo Lin, Zhonghui Tan *, Tingting Ye and Weihua Ai

College of Atmosphere and Oceanography, National University of Defense Technology, Changsha 410073, China; linjunbo20@nudt.edu.cn (J.L.); ytt1225@nudt.edu.cn (T.Y.); aiweihua@nudt.edu.cn (W.A.)
* Correspondence: tanzhonghui18@nudt.edu.cn

Highlights

What are the main findings?

- Proposing an infrared-based framework for retrieving large-scale day-night LCC from geostationary satellite observations.

What are the implications of the main findings?

- Providing a promising basis for constructing large-scale day-night LCC datasets to capture the cloud vertical structures of complex weather systems.
- Having potential value for analysis of cloud radiative effects, climate-model evaluation, and weather monitoring.

Abstract

Layered cloud cover (LCC) describes the vertical distribution of cloud occurrence and is a key variable for assessing the radiation budget of the Earth-atmosphere system. However, ground-based radars have limited spatial coverage, while existing satellite cloud-cover products rarely provide both spatiotemporal continuity and high accuracy. Because nighttime satellite observations lack visible-channel information, conventional passive satellite remote sensing remains limited in providing day-night continuous LCC retrievals. In this study, we propose an infrared-based framework for retrieving large-scale day-night LCC from geostationary satellite observations. The framework first resolves cloud vertical structure using a hybrid machine learning and physical algorithm for day-night cloud-base height (CBH) retrieval, and then derives cloud cover in different vertical layers. Validation against active measurements from spaceborne and ground-based cloud radar demonstrates that the satellite-retrieved LCC captures cloud vertical distributions and their diurnal variations. The cloud-layer identification accuracies reach 76.3% and 77.9% for daytime and nighttime, respectively, with corresponding Cohen's kappa coefficients of 0.66 and 0.68. The primary source of algorithmic uncertainty is the low precision of low-cloud identification, which is constrained by objective factors and physical characteristics. The retrieved annual mean LCC fields reproduce major climatological features, including enhanced high and deep convective clouds over the tropical western Pacific and dominant low-cloud occurrence over the mid-latitude oceans. A case study of Typhoon Doksuri further shows that the 10 min LCC retrievals capture the vertical evolution of the typhoon cloud system during intensification, eyewall structural adjustment, landfall, and post-landfall decay. These results indicate that the proposed infrared-based retrieval framework provides a promising basis for constructing large-scale day-night LCC datasets and can support cloud-radiation studies, climate-model evaluation, and weather monitoring.

Check for updates

Academic Editor: Ismail Gultepe

Received: 26 May 2026
Revised: 17 June 2026
Accepted: 23 June 2026
Published: 30 June 2026

Copyright: © 2026 by the authors. Licensee MDPI, Basel, Switzerland. This article is an open access article distributed under the terms and conditions of the Creative Commons Attribution (CC BY) license.

Keywords: layered cloud cover; geostationary satellites; cloud vertical structure; day-night retrieval; infrared remote sensing; typhoon

1. Introduction

Clouds are pivotal components of Earth's atmosphere and play an important role in regulating the radiation budget and in climate modeling [1–3]. As two fundamental macrophysical properties, cloud cover and cloud height describe the horizontal extent and vertical distribution of clouds, respectively, and therefore strongly influence the radiative budget of cloud-affected regions with cloud optical thickness (COT). High clouds generally induce atmospheric warming because they weakly reflect incoming solar radiation while emitting longwave infrared radiation at low temperatures [4,5]. The net radiative effect of high clouds is strongly modulated by cloud phase: ice clouds composed of nonspherical ice crystals exhibit different scattering and absorption properties compared to liquid water clouds, which adds complexity to their radiative forcing estimates [1,2]. By contrast, low clouds typically produce a net cooling effect in low- and mid-latitudes because they strongly reflect shortwave radiation while emitting longwave radiation at relatively high temperatures. However, during the Arctic winter, low clouds can instead exert a net warming effect due to the absence of solar radiation and their enhancement of downward longwave radiation, a process that can be further intensified by anthropogenic aerosol pollution transported from mid-latitudes [6]. More broadly, across high-latitude regions where surface temperatures are extremely low, low clouds reduce the radiative cooling of the surface and thus play a warming role in the surface energy budget [4,5]. These latitudinal and seasonal variations in cloud radiative effects underscore the importance of accurately resolving cloud vertical structure and optical properties for climate modeling.

Layered cloud cover (LCC), defined as the horizontal cloud fraction partitioned by vertical level [7,8], is a critical proxy for evaluating cloud radiative forcing and improving cloud parameterization schemes in general circulation models (GCMs). According to the European Centre for Medium-Range Weather Forecasts (ECMWF), LCC is commonly divided into high-, medium-, and low-cloud fractions, representing the horizontal fractions of clouds occurring in the corresponding tropospheric layers. Previous studies have analyzed climatological patterns by simulating LCC within atmospheric circulation frameworks. For example, the seasonal variations in radiative fluxes in Arctic regions can be reproduced accurately only when cloud cover is well simulated. Randall et al. [9] further demonstrated that global marine low cloud cover is closely coupled with variations in global mean temperature. Instead of directly providing cloud phase information, LCC complements phase-based analyses by indicating the vertical levels where clouds occur. Thereby LCC can help to localize where phase-related radiative feedbacks (e.g., ice-to-liquid transitions in mixed-phase clouds) exert their influence on the radiation budget. Although global observations and simulations suggest that clouds may exert a positive feedback, substantial and spatially non-uniform LCC biases remain among climate models, contributing to large uncertainties in future climate projections.

Consequently, accurate LCC estimation requires reliable cloud vertical structure information, particularly cloud-top height (CTH) and CBH. Ground-based instruments have been used to evaluate and constrain LCC simulations and thereby improve cloud-cover products. However, their limited spatial coverage prevents global-scale evaluation and hinders the generation of LCC datasets with continuous spatiotemporal coverage. For example, as a conventional means of ground-based observation, ground-based cloud radar can only locally obtain information on the vertical structure of clouds directly above the

station location. Geostationary satellites provide continuous meteorological observations at high spatiotemporal resolution, making them indispensable for retrieving cloud properties throughout the day and night. Nevertheless, because visible and infrared radiation has limited penetration through clouds, passive satellite radiometers mainly capture cloud-top information, which poses a major challenge for accurately retrieving cloud vertical structure [10].

Most satellite cloud-cover products are derived from cloud detection and provide only total cloud cover (TCC) in the horizontal dimension. The few satellite products that provide LCC have distinct advantages and limitations. The GOES-R satellite provides an LCC product by incorporating CTH retrievals, but the absence of essential CBH information introduces substantial uncertainty in characterizing cloud vertical distributions [11]. The NPP satellite can generate an LCC product based on both CTH and CBH, which substantially improves the retrieval of medium and low clouds. However, NPP is a polar-orbiting satellite, and its LCC product is mainly derived from daytime satellite observations, which limits its spatiotemporal coverage and broader application. Therefore, existing satellite cloud-cover products generally cannot simultaneously achieve large-scale coverage, temporal continuity, and high accuracy. Obtaining accurate LCC data with continuous spatiotemporal coverage remains a persistent challenge in cloud-property retrieval.

In recent years, numerous studies have sought to retrieve cloud properties from geostationary satellite infrared observations to improve retrieval accuracy while maintaining spatiotemporal continuity. Progress has gradually advanced from macrophysical to microphysical parameters and from single-model approaches to multi-model fusion. Yang et al. [12] constructed a unified day-night retrieval model for cloud detection, CTH, and cloud-top temperature using only the ten thermal infrared channels of Himawari-8/AHI, yet their retrieval is limited to CTH and does not provide CBH) information. Wang et al. [13] developed a thermal infrared convolutional neural network (TIR-CNN) that simultaneously retrieves cloud mask, COT, effective particle radius, and CTH from passive satellite observations without auxiliary atmospheric parameters, achieving stable diurnal performance. Extending this framework, Wang et al. [14] further demonstrated the feasibility of retrieving global CBH and cloud thermodynamic phase from thermal infrared radiometry using the same TIR-CNN architecture, with notable capability in distinguishing mixed-phase clouds characterized by ice cloud tops. In a parallel development, Huang et al. [15] proposed an optimal-estimation-based hybrid method (OE-CNN-IR) that synergistically integrates deep learning with radiative transfer simulations, using machine-learning outputs as prior states to enhance retrieval accuracy for optically thick ice clouds. Tana et al. [16] developed a machine-learning model for retrieving cloud microphysical properties from AHI infrared observations. Ye et al. [17] bridged the research gap in large-scale nighttime CBH retrieval by integrating deep learning with physical principles. The methods and results of the above studies collectively provide a promising paradigm for all-weather cloud property retrieval from passive satellite measurements. Although these studies have greatly improved the capability to obtain cloud properties from both daytime and nighttime satellite radiometer observations, day-night LCC retrieval has received comparatively little attention. The estimation of LCC requires not only accurate CTH and CBH retrievals but also robust vertical cloud classification.

This study develops a novel algorithm for retrieving large-scale day-night LCC from geostationary satellite infrared measurements. The novelty lies in constructing and validating a day-night LCC framework based on those retrieved cloud vertical-structure variables. The remainder of this paper is organized as follows: Section 2 describes the datasets, and Section 3 presents the details of the day-night LCC retrieval method. Section 4 validates

the LCC retrieval results against spaceborne and ground-based cloud radar measurements. Finally, Section 5 summarizes the main findings and discusses future perspectives.

2. Datasets

2.1. Himawari-8/9 AHI Data

The Advanced Himawari Imager (AHI) onboard the Himawari-8/9 geostationary satellites is equipped with 16 spectral channels [18] and provides high-spatiotemporal-resolution observations in the visible, near-infrared, and infrared bands. The proposed algorithm is developed using AHI infrared observations with a spatial resolution of 5 km and a temporal resolution of 10 min. Because cloud-emitted infrared radiation can be observed by satellites during both day and night, the proposed algorithm enables day-night LCC retrieval. The primary input features include infrared brightness temperatures (BTs) from AHI channels 8–16 (centered at 6.2–13.3 μm) and the satellite zenith angle (SAZ) [19,20].

2.2. MODIS Data

The Moderate Resolution Imaging Spectroradiometer (MODIS) onboard the Aqua and Terra satellites comprises 36 visible-infrared spectral channels. In this study, the Terra MODIS Collection 6.1 Level-2 cloud product is used as the label dataset for machine-learning model training. The MOD06 product provides pixel-level retrievals of cloud macrophysical and optical properties, including CTH, cloud-top pressure, cloud-top temperature, COT, cloud effective radius, and cloud water path (CWP), with a temporal resolution of 5 min and spatial resolutions of 5 km/1 km [21]. The high precision and reliability of the MOD06 cloud product have been validated through comparisons with active satellite sensors measurements [22]. Therefore, CTH and CWP from MOD06 were used as labels for machine-learning model training [21,23].

2.3. CloudSat-CALIPSO Data

The Cloud Profiling Radar (CPR) onboard CloudSat and the Cloud-Aerosol LIDAR with Orthogonal Polarization (CALIOP) onboard CALIPSO have highly complementary sensing capabilities. Their synergy is represented in the 2B-CLDCLASS-LIDAR product, which provides a more comprehensive and accurate characterization of cloud vertical structure [24]. Therefore, this study uses cloud-height and optical-property products from 2B-CLDCLASS-LIDAR to validate the feasibility and robustness of the proposed retrieval framework. However, because of a battery anomaly in 2011, CloudSat-CPR has been restricted to daylight-only operations, which precludes its use for validating nighttime performance [25].

2.4. Ka-Band Millimeter-Wave Ground-Based Cloud Radar Data

To validate the nighttime performance of the LCC retrieval algorithm, we use nighttime cloud-height observations from several Ka-band millimeter-wave ground-based cloud radar in China. These datasets, with a temporal resolution of 1 min, are used to evaluate the algorithm's capability for nighttime LCC estimation. Detailed specifications of the instruments and datasets are summarized in Table 1. The geolocations and elevations of the seven ground-based cloud radar used for LCC validation are listed in Table 2. Due to difficulties in radar data accessibility, ground-based cloud radar are distributed in China rather than globally. The nighttime validation of the algorithm's capability is regionally limited.

Table 1. Datasets used in this study.

Sensors	Products	Variables	Spatial Resolution
AHI	Level-1b	Infrared BT (centering wavelength 6.2–13.3 μm), SAZ	0.05° × 0.05°
MODIS (Terra)	MOD06_L2 (C6.1)	cloud-top height, cloud water path	5 km/1 km
ERA5	Hourly data on single levels	Skin temperature, surface pressure	0.25° × 0.25°
CPR-CALIOP	2B-CLDCLASS-LIDAR	cloud-top height, cloud-base height	1.4 × 1.7 km
Ground-based cloud radar	Cloud-height product	cloud-top height, cloud-base height	30 m (vertical)

Table 2. Geolocations and elevations of the ground-based cloud radar.

Station ID	Latitude	Longitude	Elevation
52267	41.95°N	101.07°E	940.5 m
53463	40.82°N	111.68°E	1153.5 m
53845	36.60°N	109.50°E	958.5 m
54623	39.07°N	117.73°E	4.9 m
57245	32.72°N	109.03°E	290.8 m
57461	30.73°N	111.37°E	256.5 m
57816	26.58°N	106.73°E	1223.8 m

3. Algorithm

The flowchart of the proposed day-night LCC retrieval algorithm is shown in Figure 1. First, a CBH retrieval algorithm is used to obtain accurate day-night CBH estimates from geostationary satellite measurements. Subsequently, cloudy pixels are classified into six categories according to the retrieved CTH and CBH. Finally, LCC is calculated from the pixel-level cloud classification within a 5-pixel × 5-pixel region [26].

The first step in deriving LCC is to resolve cloud vertical structure by accurately retrieving CTH and CBH. Because visible and infrared radiation has limited penetration through clouds, conventional passive satellite sensors face difficulties in capturing sub-cloud radiation, which creates a major challenge for direct CBH retrieval [17]. Previous studies have shown that CBH can be estimated as the difference between CTH and cloud geometric thickness (CGT). Tan et al. [27] developed an effective cloud water content (ECWC) look-up table (LUT), constrained by multidimensional environmental variables (e.g., surface type, latitude band, and season), to improve algorithm robustness, as shown in (1). The ECWC LUT enables daytime and nighttime CBH retrieval using CTH and CWP information. However, traditional CWP retrieval methods depend on visible channels and therefore cannot provide nighttime CWP data [21]. To address this limitation, this study adopts the nighttime CBH retrieval algorithm proposed by Ye et al. [17], which integrates deep learning with the ECWC-LUT method.

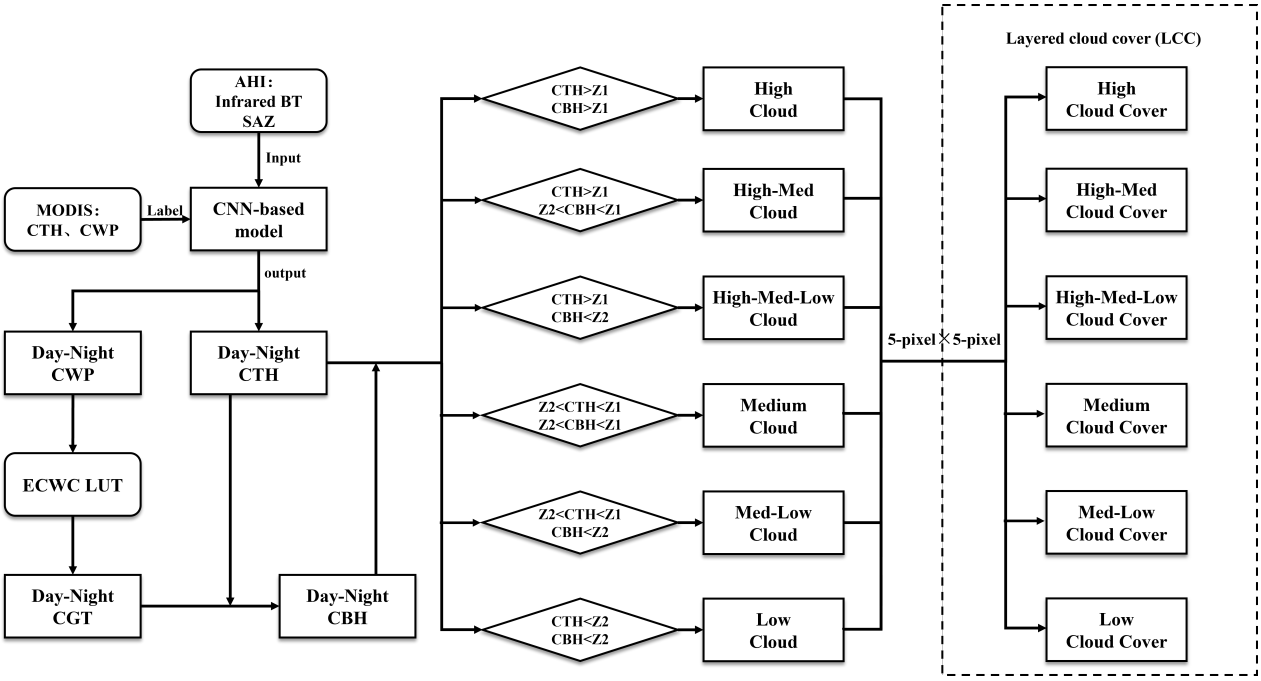


Figure 1. Flowchart of the layered cloud cover retrieval algorithm based on Advanced Himawari Imager (AHI) Level-1 infrared radiance observations.

3.1. Day-Night CTH and CWP Retrieval

The algorithm employs a convolutional neural network (CNN) based on a symmetric U-Net architecture [13]. The network inputs consist of 10 channels: the infrared brightness temperatures from AHI band 8–16 (9 channels, centered at 6.2–13.3 μm) and the satellite zenith angle (SAZ) [17], with CTH and CWP from the MOD06 product serving as training labels [18]. The model is designed to jointly predict two output variables, CTH and CWP, from a single forward pass. Spatiotemporally matched AHI-MODIS datasets divided into collocated granules were used to generate the training set (4707 samples from 2016), validation set (496 samples from 2018 at 10-day intervals), and testing sets (524 samples from 2017 and 765 samples from 2022 at 10-day intervals for comparison with CloudSat-CALIPSO, and 336 samples from 2025 for comparison with EarthCARE). The encoder extracts deep spatial and radiance-distribution features from infrared imagery using multiple layers of 3×3 convolutional kernels, while the decoder uses skip connections to fuse multi-scale spatial information. By establishing a complex nonlinear mapping between infrared observations and high-precision cloud products, this architecture enables continuous retrieval of cloud-top and optical properties during both daytime and nighttime.

3.2. Day-Night CBH Retrieval

As shown in Equation (1), using the day-night CTH and CWP retrievals, the algorithm introduces theECWC UT derived from collocated AHI-CPR-CALIOP data to estimate CBH [17,27]. First, the ECWC of a cloudy pixel is obtained from the LUT according to its CTH, CWP, and corresponding environmental conditions (i.e., latitude, season, and surface type). Subsequently, as shown in Equation (2), CGT is calculated by dividing CWP by the matched ECWC. Finally, as shown in Equation (3), day-night CBH is determined by subtracting CGT from the retrieved CTH.

$$\mathrm{ECWC} = \frac{\int_{\mathrm{CBH}}^{\mathrm{CTH}} \mathrm{CWC}(z)\, dz}{\mathrm{CTH} - \mathrm{CBH}} = \frac{\mathrm{CWP}}{\mathrm{CGT}} \tag{1}$$

$$\mathrm{CGT} = \frac{\mathrm{CWP}}{\mathrm{ECWC}} \tag{2}$$

$$\mathrm{CBH} = \mathrm{CTH} - \mathrm{CGT} \quad (3)$$

Variable definitions: CWC (cloud water content) is in g/m^3; ECWC (effective cloud water content) is in g/m^3; CTH (cloud-top height) is in km; CBH (cloud-base height) is in km; CWP (cloud water path) is in kg/m^2; and CGT (cloud geometric thickness) is in km.

According to the ECMWF definition [28], cloud layers are partitioned using surface-pressure thresholds. The boundaries between high, medium, and low clouds are defined at 0.45 and 0.8 times the surface pressure. In this study, surface pressure and skin temperature were extracted from ERA5 hourly single-level data to calculate the corresponding boundary altitudes, Z1 and Z2, over the satellite observation area. By comparing the retrieved daytime and nighttime CTH and CBH with Z1 and Z2, the cloud vertical structure is categorized into six scenarios. After this vertical classification, a pixel-level cloud-identification method is applied. Within a 5×5 pixel moving window, the horizontal fractional coverage of clouds at each altitude range is calculated as the LCC for the corresponding layer, with values ranging from 0 to 1. In this way, large-scale, day-night continuous LCC retrievals are achieved from satellite infrared observations through the synergy of machine learning and cloud physical models.

4. Results and Discussion

The day-night LCC retrievals were evaluated using the 2B-CLDCLASS-LIDAR product and ground-based cloud radar data. Because both spaceborne and ground-based cloud radars operate in a vertical-profiling mode, their measurements cannot be used directly to derive LCC. Therefore, we evaluate the accuracy of pixel-level cloud vertical-layer identification using these active measurements. This evaluation is equivalent to assessing LCC because LCC is derived from pixel-level cloud vertical-layer classifications [26].

Figure 2a–d present a typical case of CWP, CTH, CGT, and CBH retrieved from AHI infrared measurements on 23 July 2023 at 05:00 UTC. The correlation coefficients (R) for CTH and CWP are 0.93 and 0.79, respectively. The corresponding biases are -0.10 km and 0.003 kg/m^2, and the root-mean-square errors (RMSEs) are 1.92 km and 0.16 kg/m^2. The CTH and CWP retrievals agree well with the MODIS data reported by Ye et al. [17]. Specifically, Figure 2a,b show the CWP and CTH extracted from satellite infrared radiance features by the CNN-based retrieval model. The algorithm effectively captures the spatial heterogeneity of cloud-top properties across different weather systems. A highly organized tropical cyclone system is evident over the low-latitude western Pacific (near 15°N, 130°E) [29,30], where the eyewall and spiral cloud bands exhibit both extremely high cloud tops (CTH > 15 km) and abundant water content (CWP > 2.0 kg/m^2). Zonal high-cloud systems are also visible in the mid-latitude westerlies and the Intertropical Convergence Zone [31,32]. The accurate reconstruction of CWP and CTH from infrared channels overcomes the limitation caused by the absence of nighttime visible reflectance and provides reliable upstream inputs for deriving cloud vertical structure.

CGT serves as the key physical bridge linking CTH and CBH. The spatial distribution of CGT in Figure 2c is highly consistent with the dynamical characteristics of deep convective systems. In the core region of the tropical cyclone, most CGT retrievals exceed 10 km and can even exceed 14 km, corresponding to strong convection [29,30]. By contrast, in extensive cirrus regions across the tropics and mid-latitudes, the physical model reasonably derives small geometric thicknesses (CGT < 3 km) despite high CTH, owing to the extremely low CWP [31]. Figure 2d presents CBH retrievals, which are not provided by current operational geostationary satellite cloud-property products. The CBH retrievals achieve an R of 0.94 and a bias of -0.14 ± 1.26 km, indicating good agreement with daytime CloudSat-CALIPSO measurements. The algorithm's capability to capture

cloud vertical structure across the diurnal cycle is further validated by EarthCARE-CPR measurements, with biases of -0.21 ± 1.66 km and -0.35 ± 1.84 km in daytime and nighttime, respectively [17]. By combining CTH and CBH, a complete three-dimensional cloud field can be constructed using only geostationary satellite infrared measurements. On this basis, this study further classifies cloudy pixels into six categories: high cloud, high-med cloud, high-med-low cloud, medium cloud, med-low cloud, and low cloud. Figure 3 illustrates a case of the six-category cloud classification derived using the dynamic pressure-level altitude thresholds Z1 and Z2. As shown in Figure 3, the cloud distribution is primarily driven by intense thermal convection within the Intertropical Convergence Zone over the low-latitude tropical oceans (the Pacific south of 15°N) [31,33]. These systems are characterized by frequent high-med-low or high-med clouds in the troposphere.

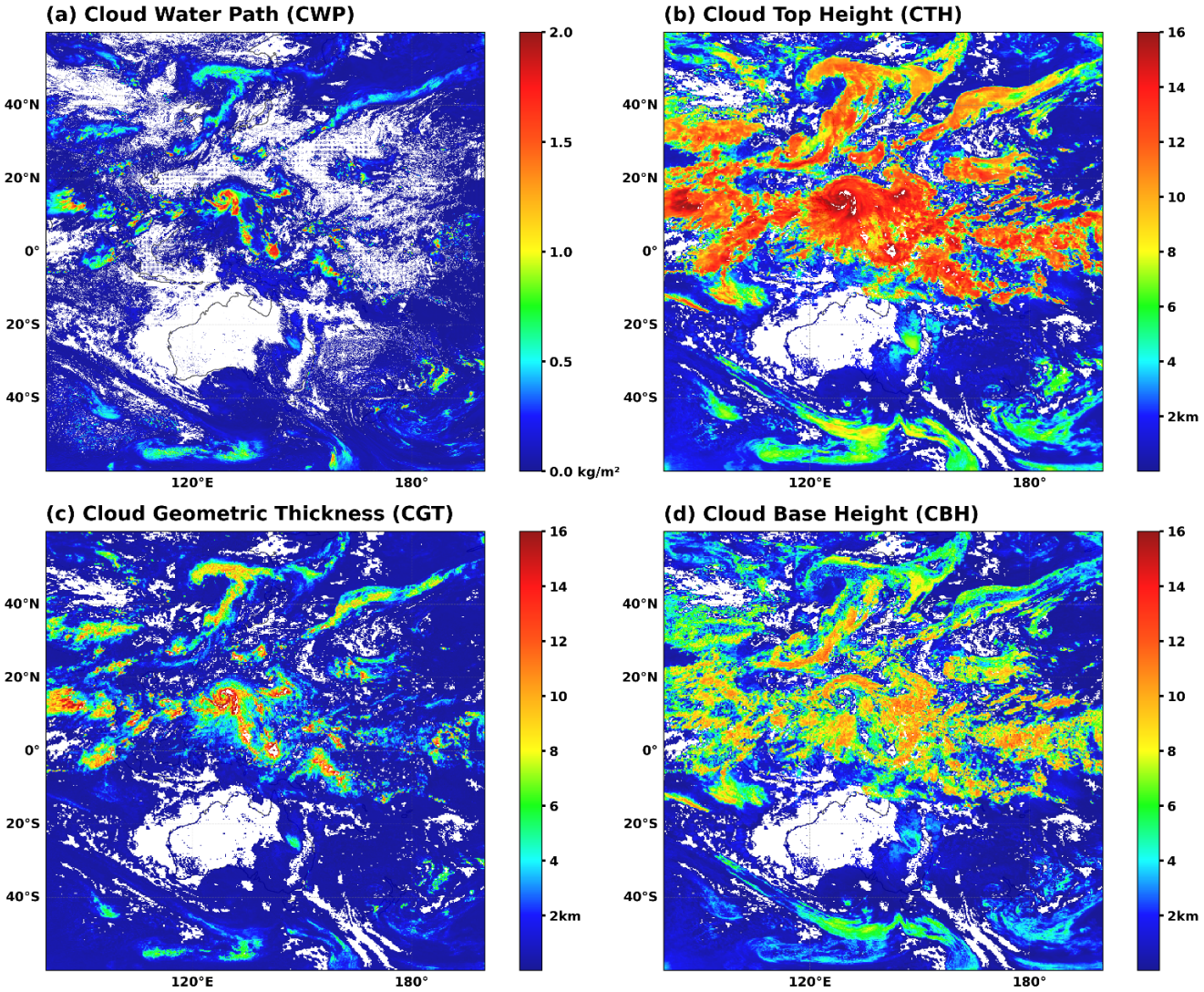


Figure 2. Spatial distributions of cloud macrophysical parameters retrieved from Himawari-8/9 AHI infrared channels on 23 July 2023 at 05:00 UTC.

The deep convective cores are surrounded by extensive cirrus anvils generated by convective dissipation, which are correctly classified as high clouds by the proposed algorithm. This spatial arrangement is consistent with the typical dynamical evolution of tropical cyclones and meso-scale convective systems (MCSs) [29,34,35]. Under the influence of baroclinic disturbances in the westerlies and large-scale atmospheric circulation, cloud types in the mid-latitudes of both hemispheres are highly interleaved and fragmented [36].

In Figure 3, these regions are characterized by a mixed distribution of medium, med-low, and high clouds.

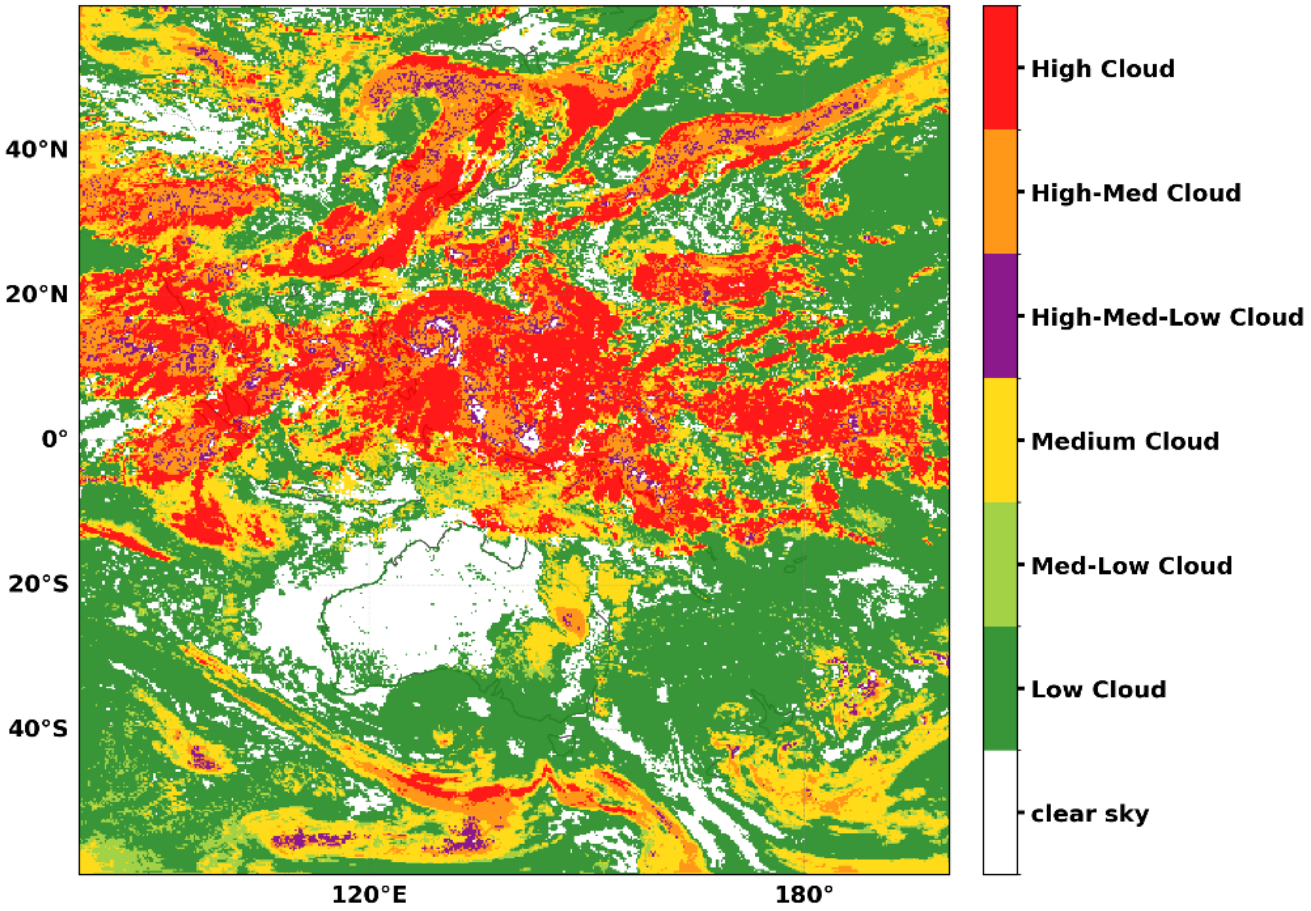


Figure 3. Cloud classification on 23 July 2023 at 05:00 UTC.

Figure 4a–d show cross-sectional comparisons between the CPR-CALIOP cloud-profile product and the AHI retrievals for two daytime cases. The results demonstrate that the passive infrared-based CTH and CBH retrievals agree well with active cloud-radar measurements and accurately depict the distribution of clouds across different vertical layers. Figure 5a–d compare the diurnal variation in cloud profiles from two ground-based cloud radars in China with the corresponding AHI retrievals. In the nighttime regions (gray shading), the AHI retrievals exhibit no data fragmentation or nonphysical jumps. Moreover, the passive infrared retrievals closely follow the cloud formation and dissipation trends observed by the ground-based radars. The vertical distributions of high, medium, and low clouds are generally consistent with the active-sensor observations, although low clouds are slightly underestimated. In regions with overlapping multi-layer clouds, the algorithm effectively infers the boundaries of obscured low and medium cloud layers, further supporting the physical reliability of the six-category cloud classification shown in Figure 3.

To quantitatively assess the performance of the proposed method, Figure 6a,b present the classification accuracies of the six AHI-derived cloud categories compared with ground-based radars measurements under daytime and nighttime conditions. Table 3 summarizes the performance metrics for the AHI six-category cloud classification. Higher precision and recall indicate fewer false alarms and missed detections, respectively. As shown in Equation (4), the F1-score is the harmonic mean of precision and recall and provides a comprehensive measure of performance for each cloud category. High clouds show the

best performance, with F1-scores of 0.893 in daytime and 0.877 in nighttime. For high-med clouds, recall is very high (0.941 in daytime and 0.879 in nighttime), whereas precision is relatively low (0.561 in daytime and 0.611 in nighttime). For high-med-low clouds, precision is very high (both above 0.95), but recall is relatively low (0.552 in daytime and 0.451 in nighttime), reflecting the physical limitation of passive remote sensing in partially underestimating vertically continuous deep convective structures. For low clouds, recall is relatively high (0.902 in daytime and 0.763 in nighttime), but precision is low (0.262 in daytime and 0.385 in nighttime). This behavior is primarily attributed to the fact that low clouds emit infrared radiation with limited penetration capability through upper cloud layers in vertically overlapping multi-layer clouds, and the infrared radiation emitted from the cloud base struggles to penetrate the cloud layer and is thus not detected by satellites in low-level convective clouds. Furthermore, strong radiative cooling of the surface often reduces the temperature difference between the lower cloud tops and the surface in nighttime [37]. This reduced contrast weakens the detection sensitivity of passive infrared sensors and is further compounded by signal attenuation in multi-layer cloud scenes.

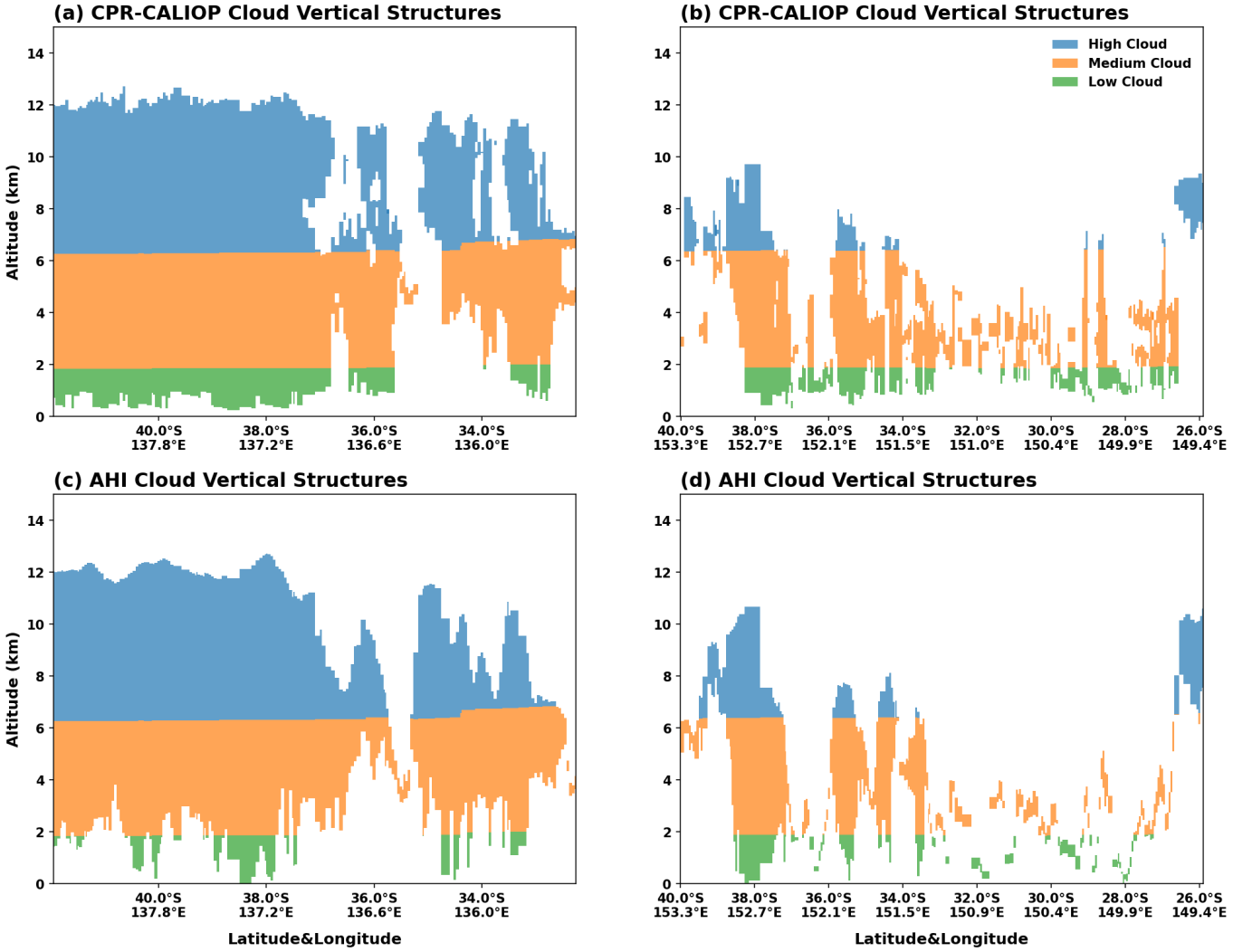


Figure 4. Daytime comparison between retrieved AHI cloud vertical structures and CPR-CALIOP 2B-CLDCLASS-LIDAR products (vertical resolution is 240 m) on (**a**,**c**) 15 March 2017 at 04:24:25 UTC (matched AHI infrared brightness temperature time at 04:20:00) and (**b**,**d**) 26 April 2017 at 03:22:19 UTC. Use the nearest neighbor matching with a spatial matching radius of $\leq$2.5 km. The matched AHI infrared BT times are 04:20:00 and 03:20:00, respectively.

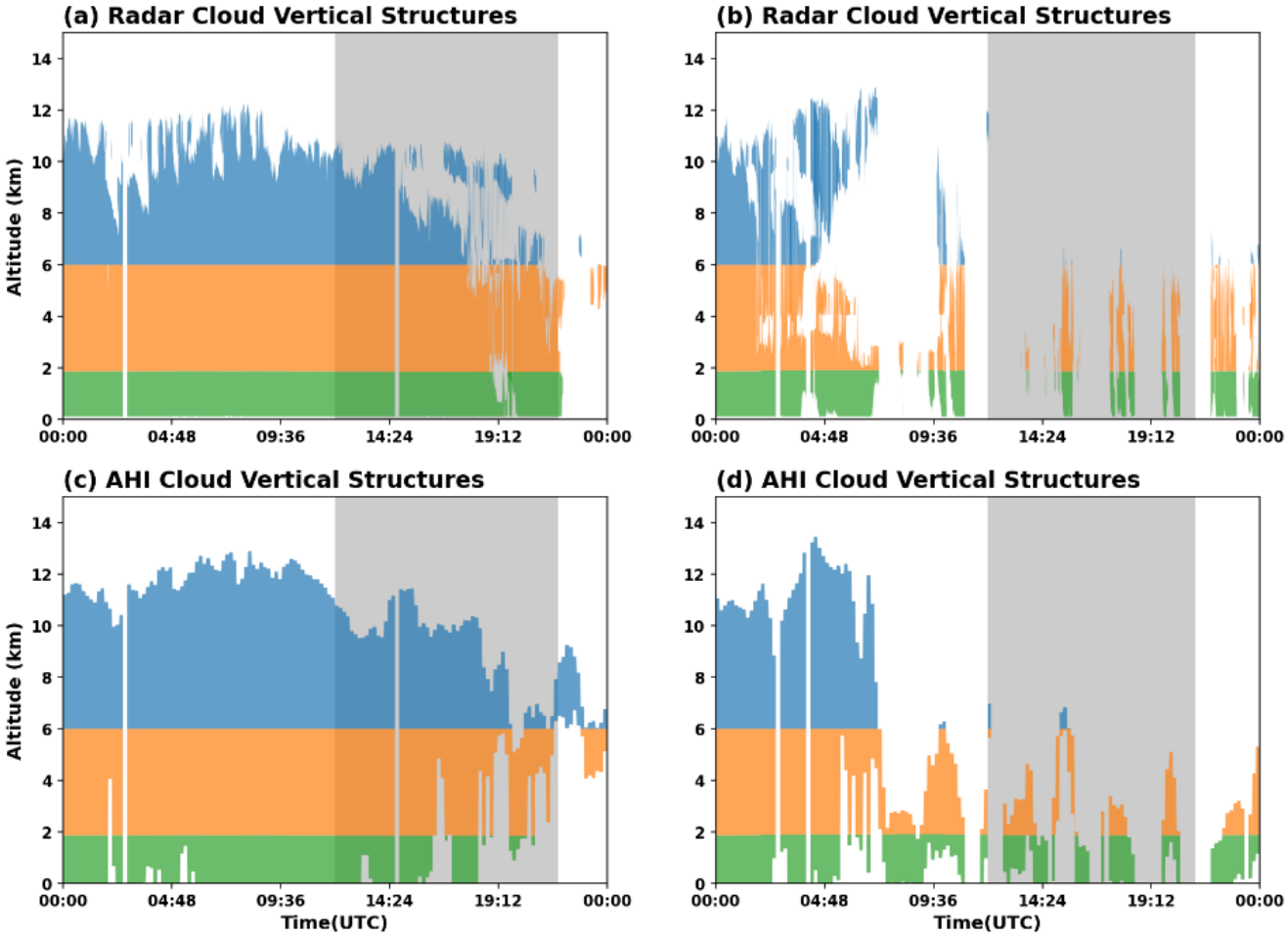


Figure 5. Comparison between retrieved AHI cloud vertical structures and ground-based radars cloud products (vertical resolution is 30 m) from (**a**,**c**) station 53845 on 28 July 2023 UTC and (**b**,**d**) station 53463 on 31 July 2023 UTC. Use the nearest neighbor matching with a spatial matching radius of $\leq$2.5 km. White and gray shading indicate daytime and nighttime conditions, respectively.

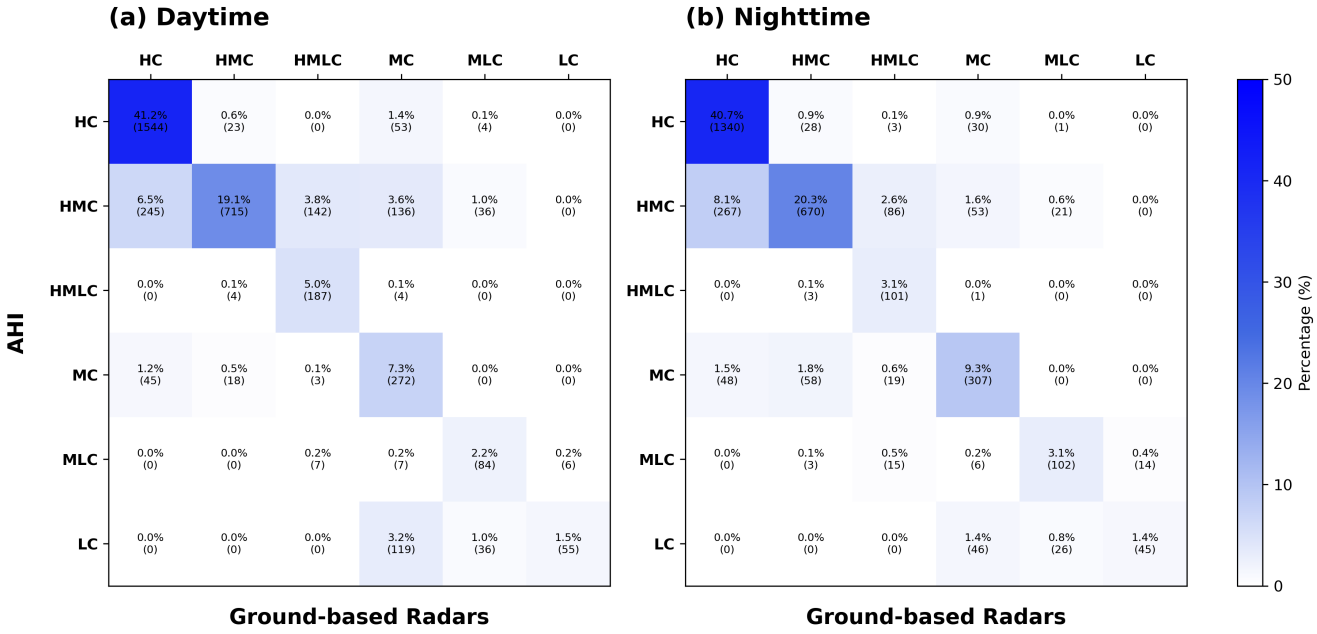


Figure 6. Confusion matrices comparing AHI-retrieved cloud classifications with measurements from six ground-based radars during (**a**) daytime and (**b**) nighttime from July 2023 to June 2024.

Overall accuracy is defined as the fraction of samples along the main diagonal of the confusion matrix. As shown in Equations (5) and (6), Cohen's kappa measures the agreement between model predictions and reference observations after removing the effect of chance agreement, with values ranging from −1 to 1. For the proposed retrievals, the overall accuracies are 76.3% in daytime and 77.9% in nighttime, with corresponding Cohen's kappa values of 0.66 and 0.68 (both greater than 0.6), indicating substantial agreement between the retrievals and reference observations. The similar color distributions in Figure 6a,b and the comparable daytime and nighttime metrics demonstrate the stability and consistency of the algorithm. The error rates above the main diagonal are higher than those below it, suggesting that the algorithm tends to underestimate CBH. In addition to objective factors, such as uncertainties in satellite-derived products, spatiotemporal mismatches between inputs and labels, and errors in the mean values of the ECWC look-up table [17], this behavior is associated with the same physical mechanism that limits low-cloud retrieval, making nighttime low-cloud retrieval a continuing challenge.

$$F_1 = 2 \times \frac{\text{Precision} \times \text{Recall}}{\text{Precision} + \text{Recall}} \tag{4}$$

$$\kappa = \frac{p_o - p_e}{1 - p_e} \tag{5}$$

$$p_e = \sum_{i=1}^{6} (p_{i+} \times p_{+i}) \tag{6}$$

Variable definitions: p_o is the observed agreement, i.e., the proportion of samples where the retrieval and reference agree; p_e is the expected agreement by chance; p_{i+} denotes the row sums divided by the total number of samples; and p_{+i} denotes the column sums divided by the total number of samples.

Table 3. Performance metrics for AHI-retrieved cloud classification based on ground-based radar validation.

Time	Type	Precision	Recall	F1-Score	Overall Accuracy	Cohen's Kappa
Daytime	HC	0.951	0.842	0.893	0.763	0.660
	HMC	0.561	0.941	0.703		
	HMLC	0.959	0.552	0.700		
	MC	0.805	0.460	0.586		
	MLC	0.808	0.525	0.636		
	LC	0.262	0.902	0.406		
Nighttime	HC	0.956	0.810	0.877	0.779	0.678
	HMC	0.611	0.879	0.721		
	HMLC	0.962	0.451	0.614		
	MC	0.711	0.693	0.702		
	MLC	0.729	0.680	0.703		
	LC	0.385	0.763	0.511		

Accurate information on cloud vertical structure is essential for analyzing the radiative impacts of clouds at different vertical levels. In Figure 7, the day-night LCC retrievals from AHI L1 infrared radiance observations during July 2023–June 2024 are used to examine annual mean spatial characteristics. Figure 7a–f present the annual mean horizontal coverage fractions of the six cloud categories. High clouds strongly absorb upward longwave radiation and emit it at low temperatures, producing a net warming effect at the top of the atmosphere. As shown in Figure 7a, high cloud cover (HCC) exhibits high values (>0.4) concentrated over the low-latitude tropics. The distribution extends from the Intertropical

Convergence Zone and the western Pacific warm pool toward the East Asian continent and the Northwest Pacific along the summer monsoon pathway [29,35]. Figure 7b,c show that both multi-layer thick clouds (high-med cloud cover, HMCC) and deep convective clouds (high-med-low cloud cover, HMLCC) have relatively low global mean fractions but enhanced occurrence in the tropics. The accurate representation of core updraft regions in strong convective systems further demonstrates the algorithm's ability to identify active convective cores [31].

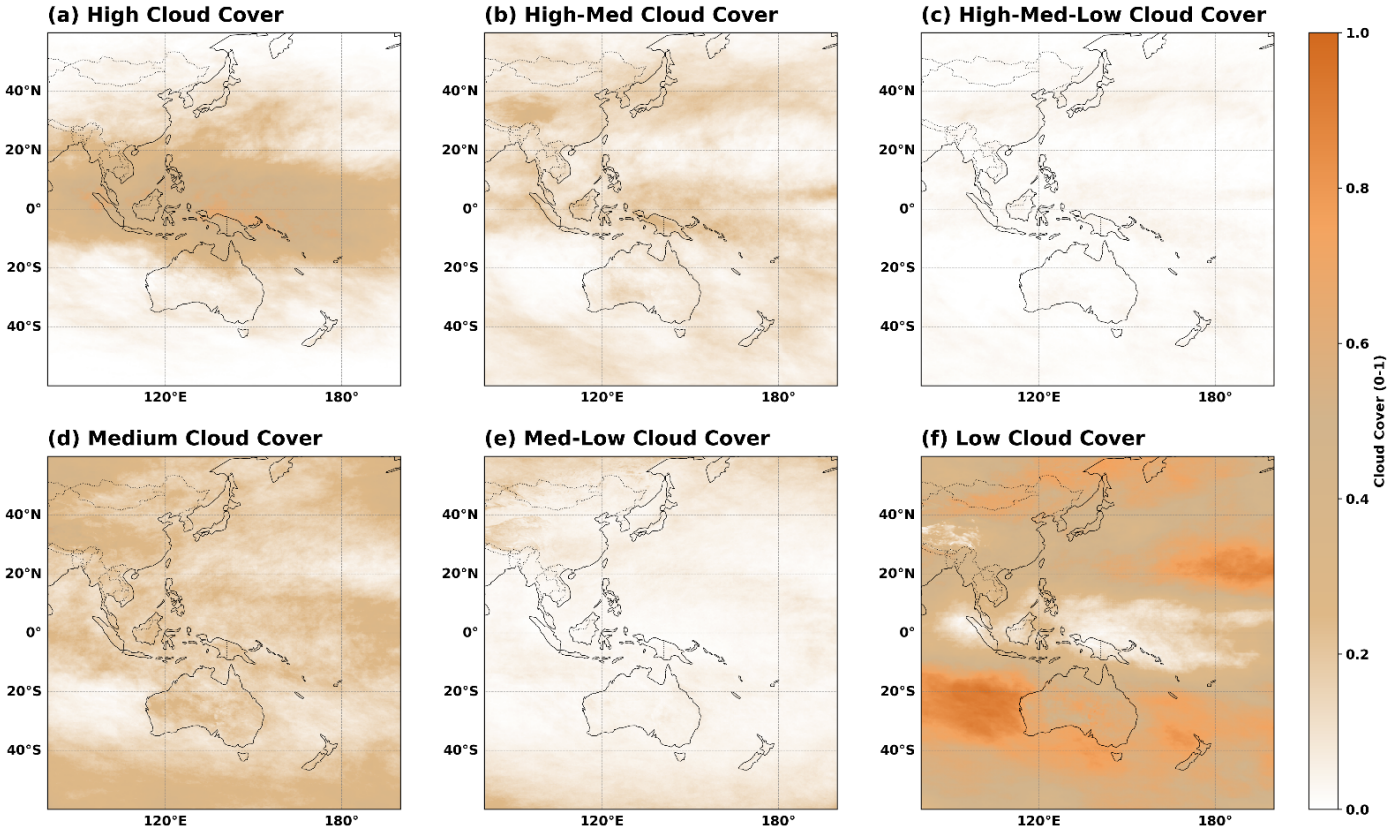


Figure 7. Annual mean LCC retrieved from Advanced Himawari Imager (AHI) measurements from July 2023 to June 2024: (**a**) high cloud cover, (**b**) high-med cloud cover, (**c**) high-med-low cloud cover, (**d**) medium cloud cover, (**e**) med-low cloud cover, and (**f**) low cloud cover.

Low clouds, which dominate the mid latitude, efficiently reflect solar radiation back to space to generate a cooling effect. Radiative characteristics exhibited by medium clouds depend on COT and underlying surface conditions. As shown in Figure 7d, the spatial distribution of medium clouds is more uniform than that of high and low clouds, but slightly higher values (0.3–0.4) appear in the westerly storm-track regions at 40°–60° latitude in both hemispheres. This pattern is closely related to extratropical cyclones and polar-front activity [36]. Figure 7f shows that low clouds dominate over the mid-latitude oceans of both hemispheres, especially over the Southern Ocean at 30°S–60°S, where annual mean cloud cover reaches 0.6 or higher. This finding is consistent with Mace et al. [38], who reported that the Southern Ocean has the highest global low-cloud occurrence based on active radar observations.

The cloud radiative effect is co-determined by cloud cover, cloud phase, COT, and CWP. Under global warming, cloud feedback changes in response to variations in LCC. Combined with retrieved cloud optical and microphysical products, our large-scale day-night LCC dataset offers a pathway to investigate cloud feedback and to evaluate how well

climate models represent the vertical distribution of clouds under different warming scenarios [5,32].

LCC can be interpreted as a horizontal representation of the vertical development and stratiform expansion of typhoon cloud systems. Figure 8 presents the 10 min mean time series of LCC retrieved from AHI within the core region of the Typhoon Doksuri cloud system (20.5°N–25°N, 118.5°E–123°E) from 26 July 2023 at 10:00 UTC to 28 July 2023 at 08:00 UTC.

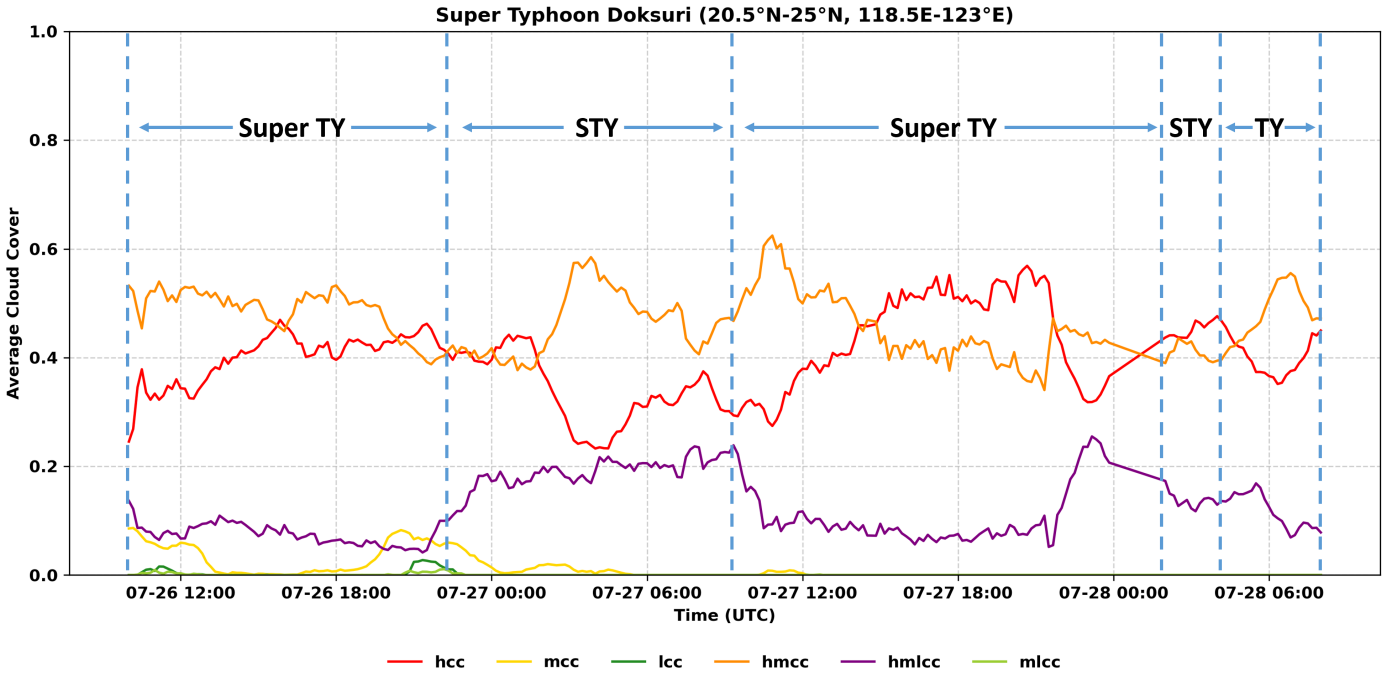


Figure 8. Ten-minute mean variations in LCC from 26 July 2023 at 10:00 UTC to 28 July 2023 at 08:00 UTC in the core region of the Typhoon Doksuri cloud system (20.5°N–25°N, 118.5°E–123°E). Super TY, STY, and TY denote super typhoon, severe typhoon, and typhoon intensity levels, respectively.

From 26 July at 10:00 UTC to 26 July at 20:00 UTC, HMCC remains relatively high while HCC exhibits an initial upward trend followed by relatively stable fluctuations, indicating that the study area was primarily influenced by the typhoon's outer spiral rainbands and deep convective cloud systems during this period. According to the Hong Kong Observatory, Doksuri weakened to a severe typhoon while traversing the northeastern South China Sea on the night of 26 July and subsequently intensified again to a super typhoon on the night of 27 July. This evolution is broadly consistent with the characteristics shown in Figure 8.

From 27 July at 00:00 UTC to approximately 28 July at 02:00 UTC, HCC and HMCC exhibit clear out-of-phase fluctuations, while HMLCC shows short-term peaks. This pattern indicates the presence of more vertically continuous cloud bodies within the typhoon inner core and outer rainbands. A multi-source observational study of Doksuri by Wang et al. [39] showed that the typhoon underwent secondary eyewall formation, concentric eyewall maintenance, and eyewall replacement before entering the South China Sea and making landfall. These processes explain the high-frequency oscillations of HCC and HMCC in Figure 8: the reorganization of the eyewall and spiral rainbands changes the relative area fractions of deep convective cloud towers, upper-level anvil clouds, and med-/low-level stratiform clouds.

On 28 July at 02:00 UTC, Doksuri made landfall near Jinjiang, Fujian Province, as a severe typhoon. HCC in the figure shows a slow upward trend and remains at 0.4–0.5.

HMCC exhibits a brief increasing trend after landfall. In contrast, HMLCC decreases markedly. This pattern likely reflects the gradual disintegration of deep convective clouds within the selected region and their transformation into a stratiform precipitation zone, residual rainbands, and an upper-level anvil cloud shield. The feature is consistent with the cloud-system evolution pattern typically observed after the main body of a typhoon makes landfall [40].

These results demonstrate that LCC not only reflects the horizontal coverage of typhoon cloud systems but also reveals changes in typhoon intensity, eyewall structural adjustment, and the vertical decoupling of cloud systems after landfall.

5. Conclusions

In this study, we developed an advanced algorithm for retrieving day-night LCC from geostationary satellite infrared observations. The algorithm first uses a CNN model to retrieve CTH and CWP from AHI infrared observations and then applies an LUT-based method to retrieve CBH for both daytime and nighttime satellite observations. The AHI cloudy pixels are subsequently classified into six categories according to their vertical distribution, and LCC is calculated from the pixel-level cloud classifications within a 5-pixel $\times$ 5-pixel region. Validation against ground-based radar measurements shows that the cloud-layer identification accuracies are 76.3% and 77.9% for daytime and nighttime, respectively, with corresponding Cohen's kappa values of 0.66 and 0.68. However, low-cloud identification has substantially low precision (0.262 in daytime and 0.385 in nighttime), reflecting the weak vertical penetration of passive infrared radiation into low clouds in multi-layer cloud systems and low-level cloud base in convective clouds at mid-to-low altitudes, the sensitivity limitations of passive infrared channels to low-level cloud-top temperatures and the influence of nocturnal radiative cooling. Despite this, the annual mean and 10 min LCC results exhibit spatiotemporal characteristics that are highly consistent with established cloud climatology. The retrievals also capture the cloud vertical structures of complex weather systems, demonstrating the reliability of the algorithm and its potential value for evaluating climate-model simulations.

Although various methods have been successfully developed for retrieving cloud properties from daytime satellite observations, this study provides a novel algorithm for inferring day-night LCC. The LCC product may be useful for evaluating climate model simulations and for supporting the development of cloud parameterization schemes, particularly in the cloud radiative effects. Moreover, the large-scale continuous LCC retrievals can be used to analyze the spatial distribution and temporal variability of three-dimensional cloud fields in weather systems such as tropical cyclones.

Nevertheless, further improvements and broader applications remain necessary. The identification accuracy for low clouds is lower than that for medium and high clouds. Craven et al. [41] have demonstrated that the lift condensation level (LCL) is an effective method for estimating the CBH of convective clouds, and it can be derived from numerical weather prediction (NWP) data. In future work, observations that fuse NWP data and reanalysis data will be introduced to optimize the determination of low-cloud locations and boundaries. In addition, we will use the cloud pixel recognition method to distinguish between single-layer and multi-layer clouds. For multi-layer cloud systems, a statistical extrapolation-based algorithm proposed by Tan et al. [26] will be applied to retrieve large-scale day-night LCC.

Relying solely on the horizontal and vertical distribution of clouds is insufficient to evaluate phase-dependent radiative feedbacks, future versions of the LCC product should be combined with cloud phase and microphysical information retrieved from the same infrared observations. Algorithm validation has thus far focused primarily on China.

The algorithm will be extended to the full disk and adapted to other geostationary satellite platforms (e.g., the FY-4 and GOES-R series), enabling the construction of a global-coverage, all-time geostationary satellite LCC dataset. Based on the method proposed in this study and the framework used to construct the analytical dataset, longer-term historical satellite data (e.g., over the past 10 years) will be processed to further investigate trends in cloud vertical distribution and the amplitude of diurnal variations in different cloud layers under global warming.

Author Contributions: Conceptualization, J.L. and Z.T.; methodology, J.L., Z.T. and T.Y.; software, J.L.; validation, J.L. and T.Y.; formal analysis, J.L.; investigation, J.L.; resources, Z.T. and W.A.; data curation, J.L. and T.Y.; writing—original draft preparation, J.L.; writing—review and editing, Z.T., T.Y. and W.A.; visualization, J.L.; supervision, Z.T. and W.A.; project administration, W.A. All authors have read and agreed to the published version of the manuscript.

Funding: This work was supported by the National Natural Science Foundation of China under Grant No. U2442215.

Data Availability Statement: The AHI data are available from the Japan Aerospace Exploration Agency (JAXA)'s P-Tree system (http://www.eorc.jaxa.jp/ptree/registration_top.html, accessed on 18 May 2024). The MODIS Collection 6.1 MOD06 dataset used in this study can be obtained from the Level-1 and Atmosphere Archive and Distribution System DAAC (https://ladsweb.modaps.eosdis.nasa.gov/search/order/2, accessed on 18 May 2025). The CPR-CALIOP 2B-CLDCLASS-LIDAR dataset can be accessed in the CloudSat Data Processing Center (https://www.cloudsat.cira.colostate.edu/order/, accessed on 14 September 2025).

Conflicts of Interest: The authors declare no conflicts of interest.

References

1. Norris, J.R.; Allen, R.J.; Evan, A.T.; Zelinka, M.D.; O'Dell, C.W.; Klein, S.A. Evidence for climate change in the satellite cloud record. *Nature* **2016**, *536*, 72–75. [CrossRef] [PubMed]
2. Baker, M.B. Cloud Microphysics and Climate. *Science* **1997**, *276*, 1072–1078. [CrossRef]
3. Sun, H.; Hu, S.; Ai, W.; Ma, S. Monte Carlo Simulation of 3D Cloud Radiance Distributions Affected by Ground-Based Lighting. *J. Geophys. Res. Atmos.* **2026**, *131*, e2025JD045501. [CrossRef]
4. Stephens, G.L. Cloud Feedbacks in the Climate System: A Critical Review. *J. Clim.* **2005**, *18*, 237–273. [CrossRef]
5. Zelinka, M.D.; Randall, D.A.; Webb, M.J.; Klein, S.A. Clearing clouds of uncertainty. *Nat. Clim. Change* **2017**, *7*, 674–678. [CrossRef]
6. Garrett, T.J.; Zhao, C. Increased Arctic cloud longwave emissivity associated with pollution from mid-latitudes. *Nature* **2006**, *440*, 787–789. [CrossRef] [PubMed]
7. Collins, W.D. Parameterization of Generalized Cloud Overlap for Radiative Calculations in General Circulation Models. *J. Atmos. Sci.* **2001**, *58*, 3224–3242. [CrossRef]
8. Meehl, G.A.; Covey, C.; Delworth, T.; Latif, M.; McAvaney, B.; Mitchell, J.F.B.; Stouffer, R.J.; Taylor, K.E. The WCRP CMIP3 Multimodel Dataset: A New Era in Climate Change Research. *Bull. Am. Meteorol. Soc.* **2007**, *88*, 1383–1394. [CrossRef]
9. Randall, D.A.; Coakley, J.A., Jr.; Lenschow, D.H.; Fairall, C.W.; Kropfli, R.A. Outlook for research on subtropical marine stratiform clouds. *Bull. Amer. Meteor. Soc.* **1984**, *65*, 1290–1301. [CrossRef]
10. Wang, J.; Rossow, W.B.; Zhang, Y. Cloud Vertical Structure and Its Variations from a 20-Yr Global Rawinsonde Dataset. *J. Clim.* **2000**, *13*, 3041–3056. [CrossRef]
11. Heidinger, A. ABI Cloud Height, Version 3.0. NOAA/NESDIS/STAR Algorithm Theoretical Basis Doc., July 2012. Available online: https://www.star.nesdis.noaa.gov/goesr/documents/ATBDs/Baseline/ATBD_GOES-R_Cloud_Height_v3.0_Jul2012.pdf (accessed on 25 September 2025).
12. Yang, Y.; Sun, W.; Chi, Y.; Yan, X.; Fan, H.; Yang, X.; Ma, Z.; Wang, Q.; Zhao, C. Machine learning-based retrieval of day and night cloud macrophysical parameters over East Asia using Himawari-8 data. *Remote Sens. Environ.* **2022**, *273*, 112971. [CrossRef]
13. Wang, Q.; Zhou, C.; Zhuge, X.; Liu, C.; Weng, F.; Wang, M. Retrieval of cloud properties from thermal infrared radiometry using convolutional neural network. *Remote Sens. Environ.* **2022**, *278*, 113079. [CrossRef]
14. Wang, Q.; Zhou, C.; Letu, H.; Zhu, Y.; Zhuge, X.; Liu, C.; Weng, F.; Wang, M. Obtaining Cloud Base Height and Phase From Thermal Infrared Radiometry Using a Deep Learning Algorithm. *IEEE Trans. Geosci. Remote Sens.* **2023**, *61*, 1–14. [CrossRef]

15. Huang, H.; Wang, Q.; Liu, C.; Zhou, C. Optimal estimation of cloud properties from thermal infrared observations with a combination of deep learning and radiative transfer simulation. *Atmos. Meas. Tech.* **2024**, *17*, 7129–7141. [CrossRef]
16. Tana, G.; Ri, X.; Shi, C.; Ma, R.; Letu, H.; Xu, J.; Shi, J. Retrieval of cloud microphysical properties from Himawari-8/AHI infrared channels and its application in surface shortwave downward radiation estimation in the sun glint region. *Remote Sens. Environ.* **2023**, *290*, 113548. [CrossRef]
17. Ye, T.; Tan, Z.; Ai, W.; Ma, S.; Zhao, X.; Hu, S.; Liu, C.; Guo, J. On the Hybrid Algorithm for Retrieving Day and Night Cloud Base Height from Geostationary Satellite Observations. *Remote Sens.* **2025**, *17*, 2469. [CrossRef]
18. Tan, Z.; Liu, C.; Ma, S.; Wang, X.; Shang, J.; Wang, J.; Ai, W.; Yan, W. Detecting Multilayer Clouds From the Geostationary Advanced Himawari Imager Using Machine Learning Techniques. *IEEE Trans. Geosci. Remote Sens.* **2022**, *60*, 1–12. [CrossRef]
19. Letu, H.; Nakajima, T.Y.; Wang, T.; Shang, H.; Ma, R.; Yang, K.; Baran, A.J.; Riedi, J.; Ishimoto, H.; Yoshida, M.; et al. A New Benchmark for Surface Radiation Products over the East Asia–Pacific Region Retrieved from the Himawari-8/AHI Next-Generation Geostationary Satellite. *Bull. Am. Meteorol. Soc.* **2022**, *103*, E873–E888. [CrossRef]
20. Iwabuchi, H.; Putri, N.S.; Saito, M.; Tokoro, Y.; Sekiguchi, M.; Yang, P.; Baum, B.A. Cloud Property Retrieval from Multiband Infrared Measurements by Himawari-8. *J. Meteor. Soc. Jpn.* **2018**, *96B*, 27–42. [CrossRef]
21. Zhuge, X.; Zou, X.; Wang, Y. AHI-Derived Daytime Cloud Optical/Microphysical Properties and Their Evaluations with the Collection-6.1 MOD06 Product. *IEEE Trans. Geosci. Remote Sens.* **2021**, *59*, 6431–6450. [CrossRef]
22. Platnick, S.; Meyer, K.G.; King, M.D.; Wind, G.; Amarasinghe, N.; Marchant, B.; Arnold, G.T.; Zhang, Z.; Hubanks, P.A.; Holz, R.E.; et al. The MODIS Cloud Optical and Microphysical Products: Collection 6 Updates and Examples from Terra and Aqua. *IEEE Trans. Geosci. Remote Sens.* **2017**, *55*, 502–525. [CrossRef] [PubMed]
23. Letu, H.; Nagao, T.M.; Nakajima, T.Y.; Riedi, J.C.; Ishimoto, H.; Baran, A.J.; Shang, H.; Sekiguchi, M.; Kikuchi, M. Ice Cloud Properties From Himawari-8/AHI Next-Generation Geostationary Satellite: Capability of the AHI to Monitor the DC Cloud Generation Process. *IEEE Trans. Geosci. Remote Sens.* **2019**, *57*, 3229–3239. [CrossRef]
24. Stephens, G.L.; Vane, D.G.; Boain, R.J.; Mace, G.G.; Sassen, K.; Wang, Z.; Illingworth, A.J.; O'Connor, E.J.; Rossow, W.B.; Durden, S.L.; et al. The CloudSat Mission and the A-Train. *Bull. Am. Meteorol. Soc.* **2002**, *83*, 1771–1790. [CrossRef]
25. Noh, Y.-J.; Forsythe, J.M.; Miller, S.D.; Seaman, C.J.; Li, Y.; Heidinger, A.K.; Lindsey, D.T.; Rogers, M.A.; Partain, P.T. Cloud-Base Height Estimation from VIIRS. Part II: A Statistical Algorithm Based on A-Train Satellite Data. *J. Atmos. Ocean. Technol.* **2017**, *34*, 585–598. [CrossRef]
26. Tan, Z.; Ma, S.; Wang, X.; Liu, Y.; Shang, J.; Wang, J.; Ai, W.; Yan, W. Estimating Layered Cloud Cover from Geostationary Satellite Radiometric Measurements: A Novel Method and Its Application. *Remote Sens.* **2022**, *14*, 5693. [CrossRef]
27. Tan, Z.; Ma, S.; Liu, C.; Teng, S.; Letu, H.; Zhang, P.; Ai, W. Retrieving Cloud Base Height from Passive Radiometer Observations via a Systematic Effective Cloud Water Content Table. *Remote Sens. Environ.* **2023**, *294*, 113633. [CrossRef]
28. Hersbach, H.; Dee, D. ERA5 reanalysis is in production. *ECMWF Newsl.* **2016**, *147*, 7.
29. Houze, R.A., Jr. Clouds in Tropical Cyclones. *Mon. Weather Rev.* **2010**, *138*, 293–344. [CrossRef]
30. Frank, W.M. The Structure and Energetics of the Tropical Cyclone I. Storm Structure. *Mon. Weather Rev.* **1977**, *105*, 1119–1135. [CrossRef]
31. Gasparini, B.; Sullivan, S.C.; Sokol, A.B.; Kärcher, B.; Jensen, E.; Hartmann, D.L. Opinion: Tropical cirrus—From micro-scale processes to climate-scale impacts. *Atmos. Chem. Phys.* **2023**, *23*, 15413–15444. [CrossRef]
32. Voigt, A.; Albern, N.; Ceppi, P.; Grise, K.; Li, Y.; Medeiros, B. Clouds, radiation, and atmospheric circulation in the present-day climate and under climate change. *Wiley Interdiscip. Rev. Clim. Change* **2021**, *12*, e694. [CrossRef]
33. Lawson, R.P.; Woods, S.; Jensen, E.; Erfani, E.; Gurganus, C.; Gallagher, M.; Connolly, P.; Whiteway, J.; Baran, A.J.; May, P.; et al. A Review of Ice Particle Shapes in Cirrus formed In Situ and in Anvils. *J. Geophys. Res. Atmos.* **2019**, *124*, 10049–10090. [CrossRef]
34. Emanuel, K. Tropical Cyclones. *Annu. Rev. Earth Planet. Sci.* **2003**, *31*, 75–104. [CrossRef]
35. Ito, K.; Miyamoto, Y.; Wu, C.-C.; Didlake, A.; Hlywiak, J.; Huang, Y.-H.; Lai, T.-K.; Pattie, L.; Qin, N.; Shimada, U.; et al. Recent Research and Operational Tools for Improved Understanding and Diagnosis of Tropical Cyclone Inner Core Structure. *J. Meteor. Soc. Jpn.* **2025**, *103*, 147–180. [CrossRef]
36. Hobbs, P.V. Organization and Structure of Clouds and Precipitation on the Mesoscale and Microscale in Cyclonic Storms. *Rev. Geophys.* **1978**, *16*, 741–755. [CrossRef]
37. Garratt, J.R.; Brost, R.A. Radiative Cooling Effects within and above the Nocturnal Boundary Layer. *J. Atmos. Sci.* **1981**, *38*, 2730–2746. [CrossRef]
38. Mace, G.G.; Zhang, Q.; Vaughan, M.; Marchand, R.; Stephens, G.; Trepte, C.; Winker, D. A description of hydrometeor layer occurrence statistics derived from the first year of merged Cloudsat and CALIPSO data. *J. Geophys. Res.* **2009**, *114*, D00A26–D00A42. [CrossRef]
39. Wang, Q.; Zhao, D.; Duan, Y.; Wang, H.; Sun, Z.; Xu, Y. Observational fine-scale evolutionary characteristics of concentric eyewall Typhoon Doksuri (2023). *Atmos. Res.* **2024**, *310*, 107630. [CrossRef]

40. Guo, R.; Yu, R.; Yang, M.; Chen, G.; Chen, C.; Chen, P.; Huang, X.; Zhang, X. Analysis of characteristics and evaluation of forecast accuracy for Super Typhoon Doksuri (2023). *Trop. Cyclone Res. Rev.* **2024**, *13*, 219–229. [CrossRef]
41. Craven, J.P.; Jewell, R.E.; Brooks, H.E. Comparison between observed convective cloud-base heights and lifting condensation level for two different lifted parcels. *Weather Forecast.* **2002**, *17*, 885–890. [CrossRef]

Disclaimer/Publisher's Note: The statements, opinions and data contained in all publications are solely those of the individual author(s) and contributor(s) and not of MDPI and/or the editor(s). MDPI and/or the editor(s) disclaim responsibility for any injury to people or property resulting from any ideas, methods, instructions or products referred to in the content.